Spin-Orbit Readout Using Thin Films of Topological Insulator Sb2Te3 Deposited by Industrial Magnetron Sputtering

Journal Article

Author(s):

Teresi, Salvatore; Sebe, Nicolas; Patterson, Jessy; Frottier, Théo; Kandazoglou, Aurélie; Noël, Paul (iD); Sgarro, Paolo; Térébénec, Damien; Bernier, Nicolas; Hippert, Françoise; Attané, Jean-Philippe; Vila, Laurent; Noé, Pierre; Cosset-Chéneau, Maxen

Spin-Orbit Readout Using Thin Films of Topological Insulator Sb$_2$Te$_3$ Deposited by Industrial Magnetron Sputtering

Salvatore Teresi, Nicolas Sebe, Jessy Patterson, Théo Frottier, Aurélie Kandazoglou, Paul Noël, Paolo Sgarro, Damien Térébénec, Nicolas Bernier, Françoise Hippert, Jean-Philippe Attané, Laurent Vila, Pierre Noé, and Maxen Cosset-Chéneau*

Driving a spin-logic circuit requires the production of a large output signal by spin-charge interconversion in spin-orbit readout devices. This should be possible by using topological insulators, which are known for their high spin-charge interconversion efficiency. However, high-quality topological insulators have so far only been obtained on a small scale, or with large scale deposition techniques that are not compatible with conventional industrial deposition processes. The nanopatterning and electrical spin injection into these materials have also proven difficult due to their fragile structure and low spin conductance. The fabrication of a spin-orbit readout device from the topological insulator Sb$_2$Te$_3$ deposited by large-scale industrial magnetron sputtering on SiO$_2$ is presented. Despite a modification of the Sb$_2$Te$_3$ layer structural properties during the device nanofabrication, a sizeable output voltage is measured that can be unambiguously ascribed to a spin-charge interconversion process. The results pave the way for the integration of layered van der Waals materials in spin-logic devices.

1. Introduction

The spin-orbit interaction induced by the spin-charge interconversion opens the way to the creation of spin-logic architectures for low power computing.[1] In these architectures, information is stored in a ferroelectric polarization state coupled to the magnetization direction of a ferromagnetic electrode. The magnetic state of the electrode is then read electrically using the spin-to-charge interconversion in either heavy metals,[2] Rashba interfaces,[3] or topological insulators.[4] In these mechanisms, the spin current produced by the ferromagnetic electrode is converted into a transverse charge current thanks to the spin orbit coupling. In order to perform spin-logic operations, the spin-orbit readout device[5] must be able to manipulate the ferroelectric polarization state of a neighboring device using its output voltage such that the devices can be cascaded.[6] Although significant progress has been made in minimizing the ferroelectric switching field,[7,8] the required voltages are still much higher than those obtained in current spin-orbit readout devices.[9–11] Therefore, their optimization becomes a major challenge for the realization of spin-logic circuits such as the magnetoelectric spin-orbit (MESO) device.[6]

Several approaches have been explored for output signal optimization of this spin-orbit readout blocks. It has been observed that downscaling the device leads to a large increase in the output signal,[10] while interface engineering is also required to improve

S. Teresi, N. Sebe, T. Frottier, A. Kandazoglou, P. Sgarro, J.-P. Attané, L. Vila, M. Cosset-Chéneau
CEA
CNRS
INP-G
Spintec
Université Grenoble Alpes
F-38054 Grenoble, France
E-mail: maxen.cosset-cheneau@orange.fr

J. Patterson, D. Térébénec, N. Bernier, P. Noé
CEA, LETI
Université Grenoble Alpes
F-38000 Grenoble, France

P. Noël
Department of Materials
ETH Zurich
CH-8093 Zurich, Switzerland

F. Hippert
CNRS
Grenoble INP
LMGP
Université Grenoble Alpes
F-38000 Grenoble, France

**ADVANCED
SCIENCE NEWS**

www.advancedsciencenews.com

**ADVANCED
FUNCTIONAL
MATERIALS**

www.afm-journal.de

the spin-injection efficiency,[9,12] and to decrease the shunting of the produced charge current.[12–14] To date, most studies have focused on heavy metals, with relatively low spin-charge interconversion efficiencies and resistivities.[15] Therefore, the next natural strategies to optimize the signal of the spin-orbit readout device is to look for materials with higher resistivities[10] and higher spin-charge interconversion efficiencies.

Topological insulators are promising materials for the realization of spin-orbit readout devices with high output voltage. These high-resistivity materials[16] are indeed known to exhibit high spin-charge interconversion efficiencies due to the Edelstein-Effect in their topological surface states,[17–19] and have already demonstrated their interest for spintronics applications in the context of the spin-orbit torque.[20] The use of these materials for spin-logic circuits is however limited by their fabrication at small-scale by MBE[17,18,21] or by mechanical exfoliation.[22,23] In addition, patterning these materials into nanoscale devices is complicated by their sensitivity to conventional nanofabrication processes,[24] so most spin-charge interconversion measurements in topological insulators have been made on microscale devices. Finally, the electrical spin injection into these materials is notoriously difficult due to intermixing effects at the interface with metals[16,25,26] and their low spin conductance caused by their semiconducting nature.[27]

Sb_2Te_3 is one of the first topological insulators discovered,[28] and is known to harbor a high spin-charge interconversion efficiency.[29] This system is also used in industry as part of phase-change memory,[30,31] which has led to the development of large-scale deposition techniques for this material,[32,33] some of which are industrially compatible, such as magnetron sputtering.[34] However, Sb_2Te_3 obtained by large-scale deposition technique has never been studied for the realization of a spin-orbit readout device.

In this paper, we demonstrate the fabrication of a spin-orbit readout device based on Sb_2Te_3 deposited using industry compatible processes on SiO_2 substrates. We show that a sizeable spin-charge interconversion signal can be obtained in this device by engineering the interface between the Sb_2Te_3 and the ferromagnetic spin-injection electrode. Finally, we discuss the effect of our nanofabrication processes on the quality of the Sb_2Te_3 film. We show that a ferromagnetic spin injection layer deposited on Sb_2Te_3 creates a stress on this material. This leads to the appearance under the ferromagnetic electrode of disorder due to stress-induced disorientation of the initially c–axis oriented Sb_2Te_3 crystallites.

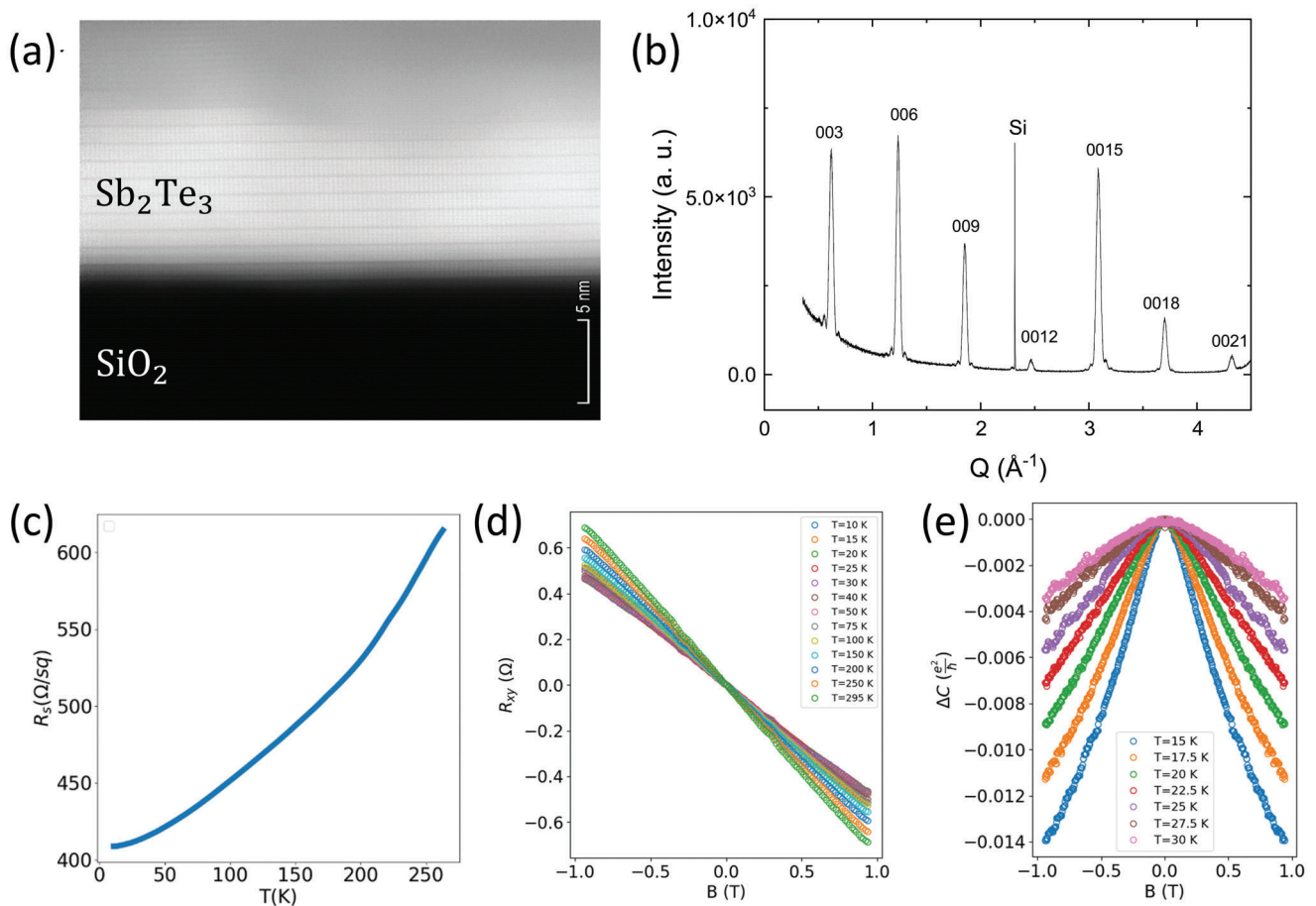## 2. Material Characterization

A 15 nm thick Sb_2Te_3 film was deposited by magnetron sputtering in an industrial cluster tool at $\approx 250\,°C$ on a 300 mm diameter (100) Si wafer, covered with a 100 nm thick thermal SiO_2 layer as a bottom insulating layer. Co-sputtering of a stoichiometric Sb_2Te_3 target and a Te target was used. As shown previously,[31,34] this deposition method compensates for Te desorption and allows to deposit well-oriented Sb_2Te_3 films, with Sb and Te planes parallel to the film surface (**Figure 1**a), due to the formation of a Te atomic layer on top of the 100 nm SiO_2 layer. Using X-ray reflectivity, the film thickness is measured to be about 15 nm, while its RMS roughness has been estimated to be 1.4 nm using

atomic force microscopy (Figure S1c, Supporting Information). The Sb_2Te_3 film was left uncapped for the purpose of being further integrated in devices, which leads to the formation of a thin oxide layer on the film surface.[35]

The structural quality of the film was controlled by X-ray diffraction (XRD) patterns acquired in the $\theta - 2\theta$ geometry (Figure 1b). Only $00l$ diffraction peaks are detected (hexagonal indexation of the rhombohedral structure of Sb_2Te_3). An in-plane diffraction pattern (Figure S1a, Supporting Information) shows that no preferred in-plane orientation of the crystallites is present. The XRD results show thus that the Sb_2Te_3 film is polycrystalline with a fiber texture. The measured hexagonal lattice parameters ($c = 3.0537(30)$ nm and $a = 0.42655(10)$ nm) are consistent with literature values.[36] The structure of Sb_2Te_3 can be described as a stacking of quintuple layers (QL) consisting of Te–Sb–Te–Sb–Te planes perpendicular to the [001] direction (hexagonal indexation) and separated by van der Waals-like gaps as visible in Figure 1a. The degree of out-of-plane orientation of the Sb_2Te_3 crystallites in the film was determined by analyzing a rocking curve shown in Figure S1b, Supporting Information. This curve can be described as the combination of a narrow peak with full width at half maximum (FWHM) of 0.8°, superimposed on a slightly broader one (FWHM of 3.8°). This indicates the coexistence of well-oriented Sb_2Te_3 crystallites, with the c–axis perpendicular to the film surface, and slightly disoriented crystallites. The detection of Laue oscillations (Figure S2, Supporting Information) indicates the high structural quality of the film. These results are comparable to the ones obtained for MBE-deposited films on amorphous layers[37] or Ge (001) substrates,[38] demonstrating the industrial potential of magnetron sputtering for the fabrication of high structural quality topological insulators on a large scale.

We then characterized the transport properties of our Sb_2Te_3 films using electrical measurements on as-deposited 15 nm thick films with gold contacts at the corners using the conventional van der Pauw method. The sheet resistance displays a metallic behavior with decreasing temperature (Figure 1c) with a resistivity of $6000\,\Omega \cdot nm$ at low temperature. This indicates that the Sb_2Te_3 bulk is conductive. A predominantly temperature-independent carrier density of $n_s = 10^{20}$ cm^{-3} with a single hole character was extracted from Hall measurements (Figure 1d), allowing us to extract a mobility of $\mu = 10$ cm$^2 \cdot$ V$^{-1} \cdot$ s^{-1} at room temperature. The metallic behavior of Sb_2Te_3 has also been observed in MBE-deposited films[39] and bulk crystals.[40] It is attributed to the presence of thermodynamically favored Sb-Te antisite defects, which push the Fermi level into the valence bands of Sb_2Te_3,[28] thus making its bulk conductive. A comparison of the transport parameter of 15 nm thick sputtered Sb_2Te_3 with literature values is reported in **Table 1**. The carrier density is one order of magnitude higher than that measured in MBE-deposited films of similar thicknesses,[29,41] indicating that our magnetron sputtering deposited films present a relatively large density of defects.[42] However, this density is closer to that obtained in MBE films of widely studied topological insulators such as Bi_2Se_3, in which a difference of two orders of magnitude in carrier density between sputtered[43,44] and MBE films[21] was observed. The mobility of our film is low compared to MBE-deposited films, which can be understood by estimating the Ioffe-Regel parameter found to be close to unity, thus indicating an intermediate level of

Figure 1. Structural and electrical characterization of the Sb_2Te_3 pristine film. a) Scanning transmission electron microscopy image acquired in high angle annular dark field (HAADF) mode and b) XRD pattern measured in the $\theta - 2\theta$ geometry using a Cu ($K_{\alpha 1}$) radiation source ($\lambda = 1.5406$ Å) as a function of $Q = 4\pi \sin(\theta)/\lambda$. The number of ≈ 1 nm thick Sb_2Te_3 quintuple layers (QLs) separated by Te-Te van der Waals gaps observed in (a) is lower than that deduced from X-ray reflectivity (XRR) because of a partial surface oxidation of the film during Focused Ion Beam (FIB) preparation of the sample lamella prior to the STEM measurement. c) Sheet resistance, d) Hall measurement signal, and e) change of conductivity versus magnetic fields measured at different temperatures. The even and odd in field signals were removed from the Hall and weak-antilocalization data, respectively.

disorder that decreases the mobility.[42] We finally performed weak-antilocalization measurements (Figure 1e). While our low field measurements do not allow us to extract the number of conduction channels, it is still possible to obtain the coherence length,[45] which was found to be 50 nm at 10 K by fitting the low field signal using the Hikami-Larkin-Nagaoka formula.[46] This length goes to zero at around 30 K (**Figure 2**e), as evidenced by the quadratic field dependence of the conductivity variation above this temperature. This dependence of the coherence length with the temperature is consistent with previous weak antilocalization measurements in Sb_2Te_3.[47]

3. Spin-Orbit Readout Device Fabrication

We then used the Sb_2Te_3 film to fabricate the spin-orbit readout device shown in Figure 2a. In this device, a ferromagnetic electrode placed on top of a T-shaped spin-orbit coupling material injects a spin current into the spin-orbit coupling material upon application of an electrical bias current across their interface (Figure 2a). This spin current is then converted into a trans-

verse charge current in the spin-orbit coupling material and detected as a transverse voltage V_{xy} (Figure 2a,b). Here, we used Sb_2Te_3 as the spin-orbit coupling material, on top of which a 20 nm thick CoFe ferromagnetic electrode is deposited. A TiO_x barrier is inserted between the Sb_2Te_3 and CoFe layers by oxidization under partial oxygen pressure of a 1 nm evaporated Ti layer. This barrier is known to promote the spin injection in materials with mismatched spin conductance.[53] The T-shape Sb_2Te_3 portion is first patterned by conventional electron beam lithography (EBL). For this purpose, the oxidized top Sb_2Te_3 layer is first removed through the EBL resist using a low energy Ion Beam Etching (IBE), and a TiO_x(1 nm)/CoFe(5 nm) hard mask is then deposited on the deoxidized Sb_2Te_3 surface by electron beam evaporation, without breaking the vacuum. All metal deposition steps are carried out using electron beam evaporation. The uncovered Sb_2Te_3 area is then removed by a soft IBE after lift-off of the hard mask. The ferromagnetic electrode is patterned in a second EBL step. A high-energy IBE is first applied to remove the CoFe oxide layer from the hard mask, before the deposition of the 20 nm thick CoFe electrode, without breaking vacuum. This procedure

**ADVANCED
SCIENCE NEWS**
www.advancedsciencenews.com

**ADVANCED
FUNCTIONAL
MATERIALS**
www.afm-journal.de

Table 1. Summary of transport parameters for topological insulators grown with different methods. MBE stands for molecular beam epitaxy and MOCVD for metal-organic chemical vapor deposition.

Material	Temperature [K]	Thickness [nm]	Resistivity [$\Omega \cdot nm$]	Mobility [$cm^2 \cdot V^{-1} \cdot s^{-1}$]	Carrier density [cm^{-3}]	Growth method	Reference
Bi_2Se_3	300	8	17 500	-	2.64×10^{19}	MBE	[48]
Bi_2Se_3	2	12	-	37	4.6×10^{19}	MBE	[49]
Bi_2Se_3	2	10	8700	130	5×10^{19}	MBE	[50]
Bi_2Se_3	300	10	13 000	80	5×10^{19}	MBE	[50]
Bi_2Se_3	5	20	4800	61	5×10^{19}	MBE	[21]
Bi_xSe_{1-x}	1.8	20	13 900	10.5	4×10^{20}	Sputtering	[43]
Bi_xSe_{1-x}	300	20	11 400	7.5	8×10^{20}	Sputtering	[43]
Bi_xSe_{1-x}	5	16	16 400	-	2.85×10^{21}	Sputtering	[44]
Sb_2Te_3	300	28	25 000	100	2.5×10^{19}	MBE	[41]
Sb_2Te_3	5	32	10 000	130	4.7×10^{19}	MOCVD	[47]
Sb_2Te_3	300	32	17 500	115	3.2×10^{19}	MOCVD	[47]
Sb_2Te_3	10	15	6000	10	1×10^{20}	Sputtering	This work
$(Bi_{0.09}Sb_{0.91})_2Te_3$	5	10	5000	60	7.3×10^{18}	MBE	[51]
$(Bi_{0.09}Sb_{0.91})_2Te_3$	300	10	7000	300	7.3×10^{18}	MBE	[51]
$(Bi_{0.12}Sb_{0.88})_2Te_3$	10	8	80 000	1900	1×10^{18}	MBE	[29]
Strained HgTe	13	20	46 000	100	5×10^{18}	MBE	[52]

ensures a good quality of spin contact through TiO_x between CoFe and Sb_2Te_3, and prevents the contact of Sb2Te3 with water and air, to which this material is sensitive. The hard mask of CoFe on Sb_2Te_3 is finally partially removed by IBE, leaving an oxidized thin TiO_x/CoFe layer on top of the region of Sb_2Te_3 which is not covered by the ferromagnetic electrode. A typical scanning microscopy image of the final device is shown in Figure 2b.
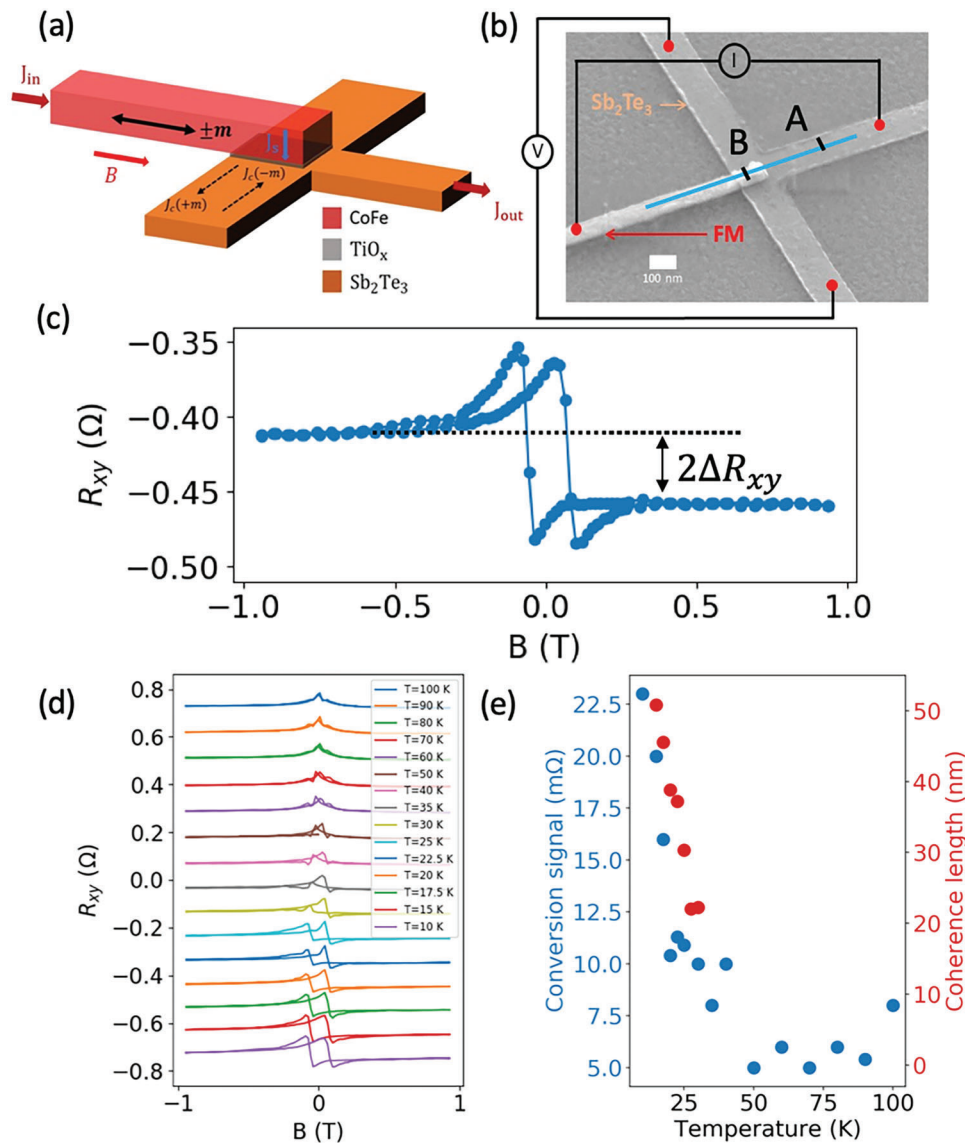
For spin-charge interconversion measurements, we used a standard lock-in amplifier (123 Hz, $I_{bias} = 100$ µA) with the connecting scheme shown in Figure 2b to measure the transverse resistance signal $R_{xy} = V_{xy}/I_{bias}$. The measurements are carried out by applying a magnetic field along the CoFe electrode (Figure 2a), thus allowing to reverse its magnetization direction. A typical transverse signal obtained at 10 K while scanning the magnetic field is shown in Figure 2c. It is constant at high field with a difference of $2\Delta R_{xy} \approx 45$ mΩ between positive and negative field values. The measured ΔR_{xy} displays a variation between 20 and 46 mΩ from device to device (see Supporting Information). The peaks at small field values can be attributed to the planar Hall effect,[11] while the baseline is possibly due to a small misalignment of the CoFe electrode with the inner leg of the Sb_2Te_3 structure.[10] It is important to note that no high-field transverse signal difference was observed in the absence of a TiO_x barrier, evidencing the importance of the barrier to avoid intermixing and/or spin conductivity mismatch. We further observed that ΔR_{xy} decreases as the temperature increases and vanishes at about 30 K while the low field signal distortions are still present (Figure 2d). ΔR_{xy} thus follows the temperature dependence of the coherence length measured in unpatterned Sb_2Te_3 (Figure 2e).

At this point, the attribution of the observed ΔR_{xy} signal to spin-charge interconversion effects deserves a comment. Indeed, the anomalous Hall effect produced by the charge current flowing vertically into the electrode may produce a signal with similar symmetries,[9,54] while the ordinary Hall effect from the stray

fields of the ferromagnetic electrode may also produce such a signal.[55] It is possible to separate these different contributions using a combination of systematic geometric dependencies and finite element simulations.[16] Here, these spurious effects can be ruled out using the temperature dependence of ΔR_{xy} (Figure 2e). As shown in Figure 1d, the Hall effect is almost temperature independent. Moreover, the anomalous Hall effect of CoFe does not vanish at 30 K.[56] Therefore, the ordinary and anomalous Hall effects cannot be at the origin of the observed transverse signal, which therefore comes from a spin-charge interconversion effect in Sb_2Te_3. The absence of transverse signal when no TiO_x barrier is present proves that a physical separation between the ferromagnetic injection electrode and the Sb_2Te_3 is necessary to avoid intermixing at the interface,[16] as well as spin-backflow and shunting in the ferromagnet.[12]

The obtained transverse resistance is slightly larger than the one found in a comparable geometry of spin-orbit readout device[16] using Bi_xSe_{1-x}. A study using heavy metal-based heterostructures reported a one order of magnitude larger transverse resistance.[10] The device scaling down used to generate this large transverse resistance in ref. [10] however resulted in a decrease in the bias current used for the measurement, and to an output voltage comparable to the one obtained in the present report. Note however that the results of refs. [10] and [16] have been obtained at room temperature.

We used finite element method simulations detailed in the Supporting Information to extract an effective spin-charge interconversion efficiency of 2 nm in Sb_2Te_3. This value is consistent with previous reports,[57] but should be regarded as an order of magnitude for the effective interconversion efficiency in Sb_2Te_3 as several parameters of our system remain currently unknown. We provide a comparison of the extracted effective interconversion efficiency in our device with literature values in **Table 2**.

**ADVANCED
SCIENCE NEWS**

www.advancedsciencenews.com

**ADVANCED
FUNCTIONAL
MATERIALS**

www.afm-journal.de

Figure 2. a) Schematic representation of the spin-orbit readout device. The charge current is injected between the ferromagnetic electrode in red and the inner leg of the T-shaped Sb_2Te_3 structure (orange). The polarization of the spin current generated at the interface between the electrode and Sb_2Te_3 is along the $\pm m$ magnetization of the electrode (black arrow). The spin-to-charge interconversion in Sb_2Te_3 creates a transverse charge current in the two outer legs of the Sb_2Te_3 structure with a sign that depends on the direction of magnetization (black dotted arrows). b) SEM image of the device presented in (a) with the connections used to flow the charge current and measure the transverse voltage V_{xy}. The A and B points correspond to the scanning transmission electron microscopy observation area presented in Figure 3. c) Transverse resistance versus magnetic field measured at 10 K using the connection configuration presented in (b). d) Evolution of the transverse resistance versus magnetic field with the temperature. e) Transverse resistance signal ΔR_{xy} and coherence length as a function of temperature.

4. Effect of the Patterning on the Sb_2Te_3 Layer Structure

It would be tempting at this point to consider that we succeeded in obtaining an interconversion signal in the topological surface states of a Sb_2Te_3 film of high structural quality. However, it is known that these materials are sensitive to nanofabrication processes that tend to create disorder. Limiting this disorder is fundamental for electrical transport to be driven by topological surface states,[42] and to achieve a high spin-charge interconversion efficiency.[17] To investigate how the nanofabrication process af-

fects the structural quality of Sb_2Te_3, we performed scanning transmission electron microscopy (STEM) measurements on our devices. This analysis was performed on two representative regions of the sample (points A and B in Figure 2b).

At point A, Sb_2Te_3 retains its structural quality as the Sb-Te quintuple layers are clearly visible (**Figure 3**a). In addition, an energy-dispersion X-ray (EDX) spectroscopy map (Figure 3c) shows that the TiO_x barrier is continuous and prevents the Te atoms from diffusing into the CoFe layer, while the Ti, Co, and Fe atoms do not diffuse into the Sb_2Te_3 layer. The EDX maps of all atomic species are shown in Figure S4, Supporting Information.

**ADVANCED
SCIENCE NEWS**

www.advancedsciencenews.com

**ADVANCED
FUNCTIONAL
MATERIALS**

www.afm-journal.de

Table 2. Summary of spin-to-charge interconversion efficiencies (λ) obtained in topological insulators using different measurement methods. SP-FMR stands for spin-pumping ferromagnetic resonance. We also added the growth method and the stack used for the measurement. Here we report the optimal value of the spin-to-charge interconversion efficiency obtained using these systems. The comparison of the spin-to-charge and charge-to-spin efficiencies remains difficult for this type of material, and a summary of the charge-to-spin efficiencies in topological insulators can be found in ref. [58].

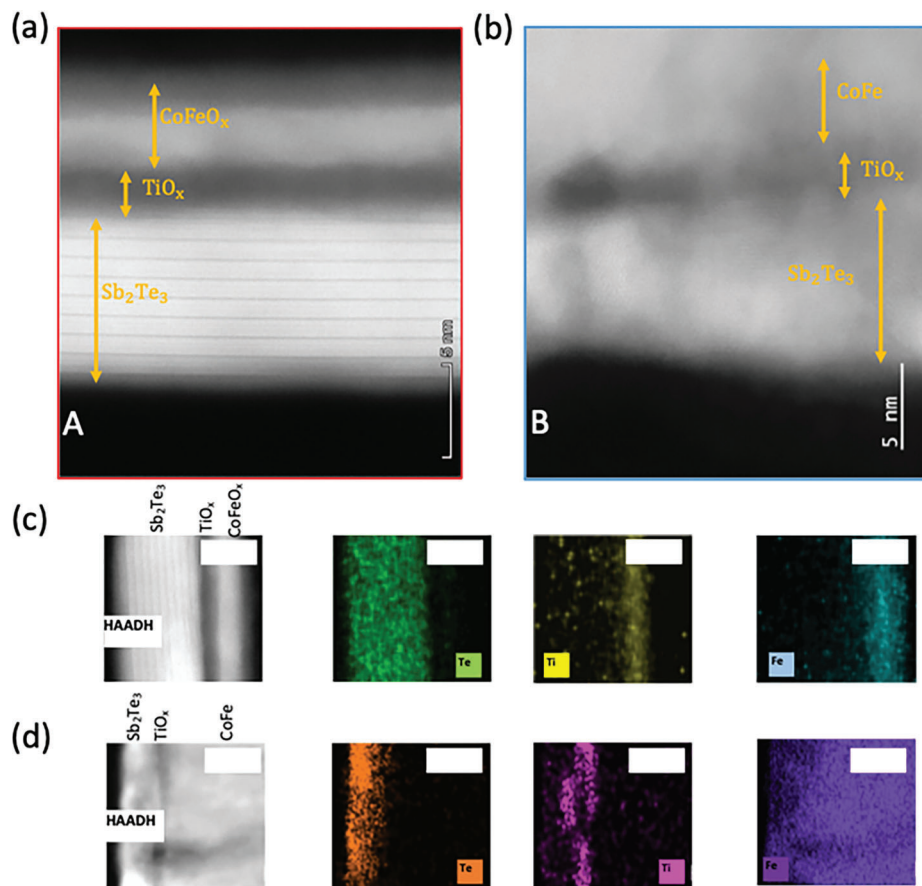| Stack	Thickness [nm]	λ [nm]	Growth method	Measurement method	Temperature [K]	Reference
α-Sn/Ag/Fe	30/2/5	2.1	MBE	SP-FMR	300	[18]
HgTe/HgCdTe/NiFe	30/1.6/20	2	MBE	SP-FMR	300	[17]
Sb_2Te_3/Au/Co/Au	30/5/5/5	0.28–0.6	MOCVD	SP-FMR	300	[57]
Bi_2Se_3/Bi/Fe	9/1/13	0.3	MBE	SP-FMR	300	[59]
Bi_2Se_3/Co	10/3	0.05	MBE	THz spectroscopy	300	[50]
$(Bi_{0.09}Sb_{0.91})_2Te_3$/NiFe	10/17	0.36	MBE	SP-FMR	300	[51]
NiFe/BiSe/Ti	15/2–16/10	0.225	Sputtering	Spin-orbit readout device	300	[16]
Sb_2Te_3/TiO_x/CoFe	15/1/20	2	Sputtering	Spin-orbit readout device	10	This work

The structure of Sb_2Te_3 under the CoFe electrode, that is, at point B (Figure 3b) where the interconversion takes place, is, however, more relevant for the spin-charge interconversion. Here, while the Sb and Te planes are still visible, they appear to be blurred and non-parallel to the plane of the substrate. This indicates that the nanofabrication process has induced the disorientation of Sb_2Te_3 grains whose c–axis is now no longer perpendicular to the substrate. In addition, the EDX maps of Figure 3d show that the continuity of the TiO_x layer has been broken in some points and that a large number of magnetic Fe atoms are present in Sb_2Te_3 (see Figures S4 and S5, Supporting Information for the extensive EDX data set).

Points A and B of the device underwent the same EBL processes and have similar in plane feature sizes. Therefore, it is likely that the lower quality of the Sb_2Te_3 film at point B compared to point A comes from their different etch/deposit history. In order to investigate the effect of the different etching and deposition steps on the structural quality of Sb_2Te_3, we performed XRD measurements in the $\theta - 2\theta$ configuration on unpatterned fullsheet samples that underwent the same etching and deposition steps as points A and B of the devices shown in Figure 2b. For this purpose, we prepared a set of three 1 cm by 1 cm macroscopic samples. Sample 1 is the 15 nm pristine Sb_2Te_3 sample that will be used as a reference. Sample 2 is the 15 nm Sb_2Te_3 film, on which the low energy IBE step used to remove the Sb_2Te_3 surface oxide was applied, followed by the deposition of the TiO_x(1 nm)/CoFe(5 nm) layer. Finally, sample 3 underwent the same process as sample 2, with the addition of a high energy etch followed by the deposition of a 20 nm thick CoFe layer. The etching and deposition history of sample 2, respectively 3, is the same as that of point A, respectively B in Figure 2b.

The measured XRD patterns are shown in **Figure 4** and Figure S6a, Supporting Information. Out-of-plane oriented Sb_2Te_3 crystallites are detected in all samples. The rocking curves of samples 1 (reference) and 2 are similar. In sample 3 the rocking curve consists of a single peak with a FWHM of 1.9°. The diffraction peaks observed in samples 1 and 2 have the same positions and widths. The only change between the two samples is an overall decrease in peak intensity in sample 2, by a factor of 1.35 compared to the reference sample (Figure S6a, Supporting Information). By contrast, large changes are observed between the XRD patterns of samples 1 and 3. A strong decrease in the intensity of the diffrac-

tion peaks is observed in sample 3 compared to the reference sample (Figure 4a). Besides, the diffraction peaks in sample 3 are observed at larger diffraction angles than in the reference and their width is larger, the latter effect being particularly marked for the peaks observed at large diffraction angles. The loss of intensity in sample 3 with respect to sample 1 can be explained by the fact that in sample 3 most of the Sb_2Te_3 crystallites are strongly tilted. Only crystallites with the c–axis close to the perpendicular to the substrate are detected in the $\theta-2\theta$ configuration used for acquisition of the XRD patterns. The small reduction of intensity between the reference and sample 2 suggests that tilted crystallites also exist in sample 2 but their number is much smaller than in sample 3. The c parameter of the Sb_2Te_3 crystallites in sample 3 is slightly smaller (by about 0.4%) than the c parameter measured in sample 1 (Figure S6b, Supporting Information). The c parameters of the samples 1 and 2 are identical. This result proves that the 20 nm thick CoFe layer in sample 3 induces a uniform strain on the out-of-plane oriented Sb_2Te_3 crystallites, whereas the thinner (5 nm thick) CoFe layer in sample 2 does not induce any significant strain effect.

Besides, a Williamson–Hall analysis of the FWHM of the diffraction peaks[60,61] (Figure 4b) shows that while the size of the Sb_2Te_3 crystallites in the direction normal to the substrate remains the same in all samples, within the limits of experimental accuracy, large inhomogenous strains are present in sample 3 but not in the reference and in sample 2. All these results show that the deposition of a 20 nm thick CoFe layer strongly alters the structural state of the Sb_2Te_3 film. It induces a strong tilt of a majority of the Sb_2Te_3 crystallites and induces uniform and non-uniform strains on the remaining out-of-plane-oriented crystallites. We therefore attribute the tilt of the Sb_2Te_3 crystallites observed in the high angle annular dark field-STEM image at point B in the device (Figure 2b) to the strain applied by the thick CoFe electrode used to inject the spin current into Sb_2Te_3. Interestingly, despite the tilt of a majority of the Sb_2Te_3 crystallites, a sizeable spin-charge interconversion signal was measured. This strain may have two detrimental effects on the measured transverse signal. We observed in Figure 3d that it results in a local breaking of the TiO_x barrier, which is expected to reduce the spin-injection efficiency and increase the shunting of the produced charge current through the ferromagnetic electrode.[12] In addition, it is possible that the formation of defects has a

ADVANCED
SCIENCE NEWS
www.advancedsciencenews.com

ADVANCED
FUNCTIONAL
MATERIALS
www.afm-journal.de

Figure 3. STEM-HAADF images of the FIB lamellae extracted at points a) A and b) B in Figure 2b. Several Sb_2Te_3 grains are visible in (b) but with no longer preferred orientation with respect to the plane of the substrate. While the thickness of the initial Sb2Te3 layer is 15 nm, only 9 QL are visible in (a). This is because of the initial removal of the Sb_2Te_3 oxide layer and the possible over-etch often present in this type of soft material. The larger thickness of the TiOx layer with respect to the nominal Ti layer thickness reported in the text is due to a combination of dilatation of the metallic layer upon oxidation, and to an uncertainty on the deposited layer thickness. c,d) HAADF images and corresponding EDX maps acquired at point A and B, respectively. The white bars correspond to 7 and 10 nm scales in (c) and (d) respectively.
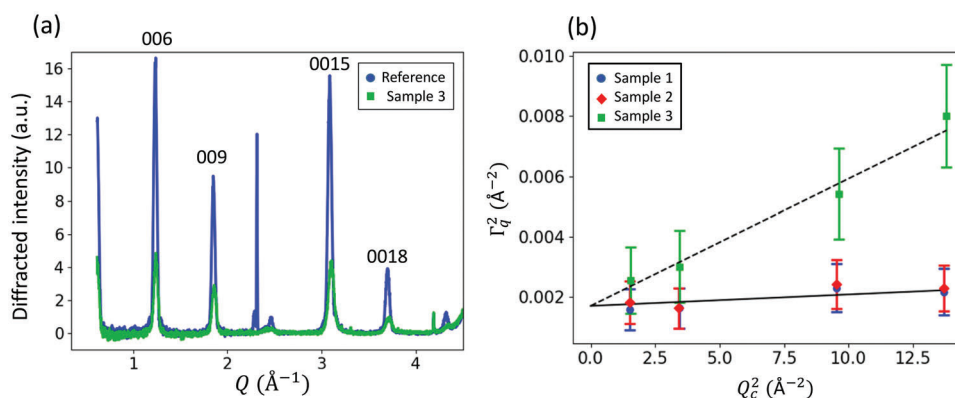
Figure 4. a) Comparison of the XRD patterns obtained for sample 1 (reference) and for sample 3 in the $\theta-2\theta$ configuration. The measurements were carried out using a Co (K_α) radiation source ($\lambda = 1.79$ Å). $Q = 4\pi\sin(\theta)/\lambda$. b) Williamson–Hall plot for the reference, samples 2 and 3. Γ_Q^2 is plotted as a function of Q_c^2 with $\Gamma_Q = (2\pi/\lambda)\cos(\theta_c)\Gamma$ and $Q_c = (4\pi/\lambda)\sin(\theta_c)$ where $2\theta_c$ is the center of a diffraction peak and Γ its FWHM in rds. The linear behavior is fitted using $\Gamma_Q^2 = \epsilon^2 Q_c^2 + (2\pi \times 0.9/D)^2$ with D the diffracting coherent domain of the Sb_2Te_3 crystallites ϵ is related to the random mean square width of the strain distribution. For the reference and sample 2, $\epsilon \approx 5 \times 10^{-3}$, while for sample 3, $\epsilon = 2 \pm 0.5 \times 10^{-2}$.

**ADVANCED
SCIENCE NEWS**

www.advancedsciencenews.com

**ADVANCED
FUNCTIONAL
MATERIALS**

www.afm-journal.de

detrimental effect on the Sb_2Te_3 spin-charge interconversion efficiency. While it is unclear how a decrease of the strain induced disorder would increase the spin-charge interconversion efficiency in Sb_2Te_3, maintaining the material structural quality during the integration into spin-logic devices will be essential for classes of materials where this parameter plays a fundamental role in the interconversion properties and functionalities, such as in ferroelectric Rashba semiconductors.[62]

5. Conclusion

In conclusion, we have presented the growth of the topological insulator Sb_2Te_3 on a large-scale using industrially compatible processes with a structural quality comparable to MBE deposited films. Furthermore, the density of defects comes closer to those of MBE-deposited films than any previous attempts to deposit topological insulators using magnetron sputtering. We then patterned Sb_2Te_3 into nanoscale spin-orbit readout devices, with a geometry compatible with the spin-orbit readout block of the MESO device. We obtained a sizeable spin-charge interconversion signal at low temperature by introducing a TiO_x barrier between the CoFe ferromagnetic electrode and the Sb_2Te_3 film. Finally, we studied the effect of our nanofabrication processes on the structural quality of the Sb_2Te_3 film. We observed that the presence of the thick CoFe layer used as a spin injection electrode creates a stress that induces disorder in the underneath Sb_2Te_3 layer.

The recent proposal of a MESO device for low energy spin-logic application has renewed the interest in spin-charge interconversion processes. New types of materials are being investigated to achieve higher spin-charge interconversion efficiencies. However, it is worth noting that while tremendous progress has been made in this area, a double challenge remains for their use in spin-orbit readout block of the MESO device. First, the materials studied must be grown on a large-scale using industrially compatible processes. Indeed, although interesting from a fundamental point of view, the fabrication of exfoliated and MBE-grown materials cannot be easily scaled up, and large-scale deposition methods must be developed. Second, interconversion studies focus primarily on microscopic[63,64] or macroscopic systems.[57,65–67] Although these methods efficiently identify materials of interest from the spin-charge interconversion point of view, their integration in nanodevices with a geometry compatible with the spin-orbit readout block of the MESO device remains scarce[16] and challenging, as illustrated in this paper.

Here, we have addressed both aspects of this problem on a specific material, Sb_2Te_3. It is clear that the disorder level in the material, as well as the nanofabrication processes, can still be optimized in order to obtain a larger spin-to-charge interconversion signal using topological surface state. In addition, other reports have observed a different temperature dependence of the interconversion in Sb_2Te_3 using different material combinations.[32] This discrepancy is probably related to different origins of the interconversion in topological insulators, where both the topological surface states, Rashba-split surface states[59] and the bulk spin Hall effect[21] can contribute to the spin-charge interconversion. It may then be possible to bring the interconversion signal observed in our device to room temperature by combining an optimization of our nanofabrication process, for instance with a re-

duction of the ferromagnetic electrode thickness to reduce the strain, with material combinations which display an interconversion signal at room temperature. Finally, these considerations are also relevant for alternative logic architectures such as the recently introduced ferroelectric spin-orbit devices[68] using the ferroelectric polarization of bulk Rashba semiconductors such as GeTe to store the information.[62] This study provides unique insights to overcome the challenges limiting the integration of the recently discovered spin-charge interconversion materials into spin-logic circuits and spin-orbit torques-based memories.

Conflict of Interest

The authors declare no conflict of interest.

Data Availability Statement

The data that support the findings of this study are available at https://doi.org/10.57745/HZDPTT.

[1] S. Manipatruni, D. E. Nikonov, I. A. Young, *Nat. Phys.* **2020**, *14*, 338.
[2] J. Sinova, S. O. Valenzuela, J. Wunderlich, C. H. Back, T. Jungwirth, *Rev. Mod. Phys.* **2015**, *87*, 1213.
[3] V. T. Pham, H. Yang, W. Y. Choi, A. Marty, I. Groen, A. Chuvilin, F. S. Bergeret, L. E. Hueso, I. V. Tokatly, F. Casanova, *Phys. Rev. B* **2021**, *104*, 184410.

[4] C. H. Li, O. M. J. van 't Erve, J. T. Robinson, Y. Liu, L. Li, B. T. Jonker, *Nat. Nanotechnol.* **2014**, *9*, 218.

[5] V. T. Pham1, L. Vila, G. Zahnd, P. Noël, A. Marty, J. P. Attané, *Appl. Phys. Lett.* **2019**, *114*, 222401.

[6] S. Manipatruni, D. E. Nikonov, C. C. Lin, T. A. Gosavi, H. Liu, B. Prasad, Y. L. Huang, E. Bonturim, R. Ramesh, I. A. Young, *Nature* **2019**, *565*, 35.

[7] B. Prasad, Y. L. Huang, R. V. Chopdekar, Z. Chen, J. Steffes, S. Das, Q. Li, M. Yang, C. C. Lin, T. Gosavi, D. E. Nikonov, Z. Q. Qiu, L. W. Martin, B. D. Huey, I. Young, J. Íñiguez, S. Manipatruni, R. Ramesh, *Adv. Mater.* **2020**, *32*, 2001943.

[8] R. Ramesh, S. Manipatruni, *Proc. R. Soc. A* **2021**, *477*, 20200942.

[9] V. T. Pham, L. Vila, G. Zahnd, A. Marty, W. Savero-Torres, M. Jamet, J. P. Attané, *Nano Lett.* **2016**, *16*, 6755.

[10] V. T. Pham, I. Groen, S. Manipatruni, W. Y. Choi, D. E. Nikonov, E. Sagasta, C. C. Lin, T. A. Gosavi, A. Marty, L. E. Hueso, I. A. Young, F. Casanova, *Nat. Electron.* **2020**, *3*, 309.

[11] H. Mizuno, H. Isshiki, K. Kondou, Y. Zhu, Y. Otani, *Appl. Phys. Lett.* **2021**, *119*, 092401.

[12] V. T. Pham, M. Cosset-Chéneau, A. Brenac, O. Boulle, A. Marty, J. P. Attané, L. Vila, *Phys. Rev. B* **2021**, *103*, L201403.

[13] M. Cosset-Chéneau, M. Husien Fahmy, A. Kandazoglou, C. Grezes, A. Brenac, S. Teresi, P. Sgarro, P. Warin, A. Marty, V. T. Pham, J. P. Attané, L. Vila, *Phys. Rev. B* **2022**, *106*, L220405.

[14] L. Liu, R. A. Buhrman, D. C. Ralph, *arXiv:1111.3702v3* **2012**.

[15] J. C. Rojas-Sánchez, A. Fert, *Phys. Rev. Appl.* **2019**, *11*, 054049.

[16] W. Y. Choi, I. C. Arango, V. T. Pham, D. C. Vaz, H. Yang, I. Groen, C. C. Lin, E. S. Kabir, K. Oguz, P. Debashis, J. J. Plombon, H. Li, D. E. Nikonov, A. Chuvilin, L. E. Hueso, I. A. Young, F. Casanova, *Nano Lett.* **2022**, *22*, 7992.

[17] P. Noel, C. Thomas, Y. Fu, L. Vila, B. Haas, P. H. Jouneau, S. Gambarelli, T. Meunier, P. Ballet, J. P. Attané, *Phys. Rev. Lett.* **2018**, *120*, 167201.

[18] J. C. Rojas-Sánchez, S. Oyarzún, Y. Fu, A. Marty, C. Vergnaud, S. Gambarelli, L. Vila, M. Jamet, Y. Ohtsubo, A. Taleb-Ibrahimi, P. Le Fèvre, F. Bertran, N. Reyren, J. M. George, A. Fert, *Phys. Rev. Lett.* **2016**, *116*, 096602.

[19] H. Wang, J. Kally, J. S. Lee, T. Liu, H. Chang, D. R. Hickey, K. A. Mkhoyan, M. Wu, A. Richardella, N. Samarth, *Phys. Rev. Lett.* **2016**, *117*, 076601.

[20] J. Han, L. Liu, *APL Mater.* **2021**, *9*, 060901.

[21] P. Deorani, J. Son, K. Banerjee, N. Koirala, M. Brahlek, S. Oh, H. Yang, *Phys. Rev. B* **2014**, *90*, 094403.

[22] J. Tian, S. Hong, I. Miotkowski, S. Datta, Y. P. Chen, *Sci. Adv.* **2017**, *3*, e1602531.

[23] A. Dankert, J. Geurs, M. V. Kamalakar, S. Charpentier, S. P. Dash, *Nano Lett.* **2015**, *15*, 7976.

[24] C. H. Li, O. M. J. van 't Erve, Y. Y. Li, L. Li, B. T. Jonker, *Sci. Rep.* **2016**, *6*, 29533.

[25] F. Bonell, M. Goto, G. Sauthier, J. F. Sierra, A. I. Figueroa, M. V. Costache, S. Miwa, Y. Suzuki, S. O. Valenzuela, *Nano Lett.* **2020**, *20*, 5893.

[26] L. A. Walsh, C. M. Smyth, A. T. Barton, Q. Wang, Z. Che, R. Yue, J. Kim, M. J. Kim, R. M. Wallace, C. L. Hinkle, *Phys. Chem. C* **2017**, *121*, 23551.

[27] A. Fert, H. Jaffrès, *Phys. Rev. B* **2021**, *64*, 184420.

[28] D. Hsieh, Y. Xia, D. Qian, L. Wray, F. Meier, J. H. Dil, J. Osterwalder, L. Patthey, A. V. Fedorov, H. Lin, A. Bansil, D. Grauer, Y. S. Hor, R. J. Cava, M. Z. Hasan, *Phys. Rev. Lett.* **2009**, *103*, 146401.

[29] K. Kondou, R. Yoshimi, A. Tsukazaki, Y. Fukuma, J. Matsuno, K. S. Takahashi, M. Kawasaki, Y. Tokura, Y. Otani, *Nat. Phys.* **2016**, *12*, 1027.

[30] D. Térébénec, N. Castellani, N. Bernier, V. Sever, P. Kowalczyk, M. Bernard, M. C. Cyrille, N. P. Tran, F. Hippert, P. Noé, *Phys. Status Solidi RRL* **2021**, *15*, 2000538.

[31] P. Kowalczyk, F. Hippert, N. Bernier, C. Mocuta, C. Sabbione, W. Batista-Pessoa, P. Noé, *Small* **2018**, *14*, 1704514.

[32] E. Longo, L. Locatelli, M. Belli, M. Alia, A. Kumar, M. Longo, M. Fanciulli, R. Mantovan, *Adv. Mater. Interfaces* **2021**, *8*, 2101244.

[33] M. Rimoldi, R. Cecchini, C. Wiemer, A. Lamperti, E. Longo, L. Nasi, L. Lazzarini, R. Mantovan, M. Longo, *RSC Adv.* **2020**, *10*, 19936.

[34] F. Hippert, P. Kowalczyk, N. Bernier, C. Sabbione, X. Zucchi, D. Térébénec, C. Mocuta, P. Noé, *J. Phys. D: Appl. Phys.* **2020**, *53*, 154003.

[35] P. Noel, Ph.D. Thesis, Université Grenoble Alpes, **2019**.

[36] T. L. Anderson, H. N. Krause, *Acta Crystallogr., Sect. B: Struct. Sci., Cryst. Eng. Mater.* **1974**, *30*, 1307.

[37] J. E. Boschker, E. Tisbi, E. Placidi, J. Momand, A. Redaelli, B. J. Kooi, F. Arciprete, R. Calarco, *AIP Adv.* **2017**, *7*, 015106.

[38] B. Zheng, Y. Sun, J. Wu, M. Han, X. Wu, K. Huang, S. Feng, *J. Phys. D: Appl. Phys.* **2017**, *50*, 105303.

[39] J. Zhang, C. Z. Chang, Z. Zhang, J. Wen, X. Feng, K. Li, M. Liu, K. He, L. Wang, X. Chen, Q. K. Xue, X. Ma, Y. Wang, *Nat. Commun.* **2011**, *2*, 574.

[40] R. Sultana, G. Gurjar, S. Patnaik, V. P. S. Awana, *Mater. Res. Express* **2018**, *5*, 046107.

[41] X. Zhang, Z. Zeng, C. Shen, Z. Zhang, Z. Wang, C. Lin, Z. Hu, *J. Appl. Phys.* **2014**, *115*, 024307.

[42] M. Brahlek, N. Koirala, N. Bansal, S. Oh, *Solid State Commun.* **2015**, *215*, 54.

[43] P. Sahu, J. Y. Chen, J. C. Myers, J. P. Wang, *Appl. Phys. Lett.* **2018**, *112*, 122402.

[44] D. C. Mahendra, T. Liu, J. Y. Chen, T. Peterson, P. Sahu, H. Li, Z. Zhao, M. Wu, J. P. Wang, *Appl. Phys. Lett.* **2019**, *114*, 102401.

[45] J. Dufouleur, L. Veyrat, B. Dassonneville, C. Nowka, S. Hampel, P. Leksin, B. Eichler, O. G. Schmidt, B. Büchner, R. Giraud, *Nano Lett.* **2016**, *16*, 6733.

[46] S. Hikami, A. I. Larkin, Y. Nagaoka, *Prog. Theor. Phys.* **1980**, *63*, 707.

[47] L. Locatelli, A. Kumar, P. Tsipas, A. Dimoulas, R. Mantovan, *Sci. Rep.* **2022**, *12*, 3891.

[48] A. R. Mellnik, J. S. Lee, A. Richardella, J. L. Grab, P. J. Mintun, M. H. Fischer, A. Vaezi, A. Manchon, E. A. Kim, N. Samarth, D. C. Ralph, *Nature* **2014**, *511*, 449.

[49] T. Guillet, A. Marty, C. Beigné, C. Vergnaud, M. T. Dau, P. Noel, J. Frigerio, G. Isella, J. Jamet, *AIP Adv.* **2018**, *8*, 115125.

[50] X. Wang, L. Cheng, D. Zhu, Y. Wu, M. Chen, Y. Wang, D. Zhao, C. B. Boothroyd, Y. M. Lam, J. X. Zhu, M. Battiato, J. C. W. Song, H. Yang, E. E. M. Chia, *Adv. Mater.* **2018**, *30*, 1802356.

[51] S. H. Su, P. Y. Chuang, J. C. Lee, C. W. Chong, Y. W. Li, Z. M. Lin, Y. C. Chen, C. M. Cheng, J. C. A. Huang, *ACS Appl. Electron. Mater.* **2021**, *3*, 72988.

[52] Y. Fu, J. Li, J. Papin, P. Noel, S. Teresi, M. Cosset-Chéneau, C. Grezes, T. Guillet, C. Thomas, Y. M. Niquet, P. Ballet, T. Meunier, J. P. Attané, A. Fert, L. Vila, *Nano Lett.* **2022**, *22*, 7867.

[53] P. J. Zomer, M. H. D. Guimarães, N. Tombros, B. J. van Wees, *Phys. Rev. B* **2012**, *86*, 161416(R).

[54] I. Groen, V. T. Pham, N. Leo, A. Marty, L. E. Hueso, F. Casanova, *Phys. Rev. Appl.* **2021**, *15*, 044010.

[55] E. K. de Vries, A. M. Kamerbeek, N. Koirala, M. Brahlek, M. Salehi, S. Oh, B. J. van Wees, T. Banerjee, *Phys. Rev. B* **2016**, *92*, 201102(R).

[56] Y. Omori, E. Sagasta, Y. Niimi, M. Gradhand, L. E. Hueso, F. Casanova, Y. Otani, *Phys. Rev. B* **2019**, *99*, 014403.

[57] E. Longo, M. Belli, M. Alia, M. Rimoldi, R. Cecchini, M. Longo, C. Wiemer, L. Locatelli, P. Tsipas, A. Dimoulas, G. Gubbiotti, M. Fanciulli, R. Mantovan, *Adv. Funct. Mater.* **2022**, *32*, 2109361.

[58] Y. Wang, H. Yang, *Acc. Mater. Res.* **2022**, *3*, 1061.

[59] R. Sun, S. Yang, X. Yang, E. Vetter, D. Sun, N. Li, L. Su, Y. Li, Y. Li, Z. Z. Gong, Z. K. Xie, K. Y. Hou, Q. Gul, W. He, X. Q. Zhang, Z. H. Cheng, *Nano Lett.* **2019**, *19*, 4420.

[60] G. K. Williamson, W. H. Hall, *Acta Metall.* **1953**, *1*, 22.

[61] F. Hippert, P. Kowalczyk, N. Bernier, C. Sabbione, X. Zucchi, D. Térébénec, C. Mocuta, P. Noé, *J. Phys. D: Appl. Phys.* **2020**, *53*, 154003.

[62] S. Varotto, L. Nessi, S. Cecchi, J. Sławińska, P. Noël, S. Petrò, F. Fagiani, A. Novati, M. Cantoni, D. Petti, E. Albisetti, M. Costa, R. Calarco, M. Buongiorno Nardelli, M. Bibes, S. Picozzi, J. P. Attané, L. Vila, R. Bertacco, C. Rinaldi, *Nat. Electron.* **2021**, *4*, 740.

[63] L. Liu, A. Richardella, I. Garate, Y. Zhu, N. Samarth, C. T. Chen, *Phys. Rev. B* **2015**, *91*, 235437.

[64] L. A. Benitez, W. Savero Torres, J. F. Sierra, M. Timmermans, J. H. Garcia, S. Roche, M. V. Costache, S. O. Valenzuela, *Nat. Mater.* **2020**, *19*, 170.

[65] D. C. Mahendra, J. Y. Chen, T. Peterson, P. Sahu, B. Ma, N. Mousavi, R. Harjani, J. P. Wang, *Nano Lett.* **2019**, *19*, 4836.

[66] L. M. Vincente-Arche, S. Mallik, M. Cosset-Cheneau, P. Noël, D. C. Vaz, F. Trier, T. A. Gosavi, C. C. Lin, D. E. Nikonov, I. A. Young, A. Sander, A. Barthélémy, J. P. Attané, L. Vila, M. Bibes, *Phys. Rev. Mater.* **2021**, *5*, 064005.

[67] H. He, L. Tai, D. Wu, H. Wu, A. Razavi, K. Wong, Y. Liu, K. L. Wang, *APL Mater.* **2021**, *9*, 071104.

[68] P. Noël, F. Trier, L. M. Vicente Arche, J. Bréhin, D. C. Vaz, V. Garcia, S. Fusil, A. Barthélémy, L. Vila, M. Bibes, J. P. Attané, *Nature* **2020**, *580*, 483.